Spectroscopic Microtomography in the Visible Wavelength Range

Yongjin Sung[*]
College of Engineering & Applied Science, University of Wisconsin, Milwaukee, Wisconsin 53211, USA

(Received 29 August 2018; revised manuscript received 25 October 2018; published 19 November 2018)

We demonstrate spectroscopic microtomography in the visible wavelength range (450–700 nm) using digital holographic tomography, a wavelength-scanning source, and a variable-optical-path-length strategy. This multidimensional imaging system can directly measure the absorption-coefficient and refractive-index spectra of a three-dimensional specimen. We apply the system developed to characterize three types of polystyrene beads (undyed, blue dyed, and red dyed) as well as oxygenated and deoxygenated single red blood cells.

DOI: 10.1103/PhysRevApplied.10.054041

I. INTRODUCTION

Spectroscopic microtomography measures a four-dimensional hyperspectral data cube, the absorption spectrum at each voxel within a three-dimensional microscopic specimen. Numerous spectroscopic techniques can provide the total attenuation by or absorbance of a specimen in the visible wavelength range. However, only a few have depth-sectioning capability. For example, spectroscopic optical coherence tomography uses coherence gating to resolve depth and has been applied to *in vivo* functional imaging [1,2]. Confocal light absorption and scattering spectroscopic microscopy detects and characterizes small structures beyond the diffraction limit [3]. Spectroscopic microtomography has also been demonstrated in the x-ray [4,5] and infrared [6,7] ranges with use of synchrotron radiation [5,6] and recently with tabletop sources [4,4]. X-ray imaging can provide the electronic structure of a specimen with high spatial resolution, whereas infrared imaging can reveal rich molecular fingerprints of a specimen by exciting numerous vibrational modes.

Here we demonstrate spectroscopic microtomography in the visible wavelength range (450–700 nm) using digital holographic tomography (DHT) together with a wavelength-scanning source and a variable-optical-path-length strategy. DHT typically measures the three-dimensional refractive-index map of a transparent specimen by scanning the illumination angle, rotating the sample, or scanning the objective-lens focus [8–13]. For the demonstration, Shack-Hartmann sensors [13], interferometers [8–11], and transport-of-intensity methods [12] have been used. Several efforts have recently been made to perform DHT at multiple wavelengths [14,15]. Of note, previous work focused on measuring the refractive index of a specimen using only the phase information, while the absorption information is discarded or used only for numerical propagation of the measured light field. The refractive index and the absorption constant can be calculated from the real part and the imaginary part, respectively, of the susceptibility, which is causal. Thus, they are related by the Kramers-Kronig relations; one spectrum measured over a sufficiently broad range determines the other spectrum. With use of these relations, the refractive-index spectrum of hemoglobin solution was estimated from a measured absorption spectrum [16–18]. Here we directly measure the four-dimensional absorption and refractive-index maps without relying on the Kramers-Kronig relations.

II. METHODS

We build a visible spectroscopic microtomography system on an off-axis Mach-Zehnder interferometer, which has been widely used for digital holographic imaging [19]. Figure 1(a) shows a schematic diagram of the setup. For the light source, we use a supercontinuum laser (NKT Photonics, WL SC400-4) coupled with a tunable filter (NKT Photonics, LLTF-VIS). After the tunable filter, there is single-mode laser light at a selected wavelength in the range from 400 to 1000 nm and with a bandwidth (FWHM) of 1.0–2.5 nm. The laser beam is collimated with use of an objective lens (Mitutoyo, ×10 M Plan APO) and then split by beam splitter BS1 into two beams: one passing through the sample, and thus called the “sample beam,” and the other, called the “reference beam,” propagating in the free space. For the condenser and objective lenses, we use the same ×100, 1.3-numerical-aperture lenses (Olympus, UPlanFl). The reference beam is combined with the sample beam after beam splitter BS2. BS2 is slightly rotated to tilt the reference beam with respect to the sample beam and generate an interferogram with

---

[*] yongjin.sung@gmail.com

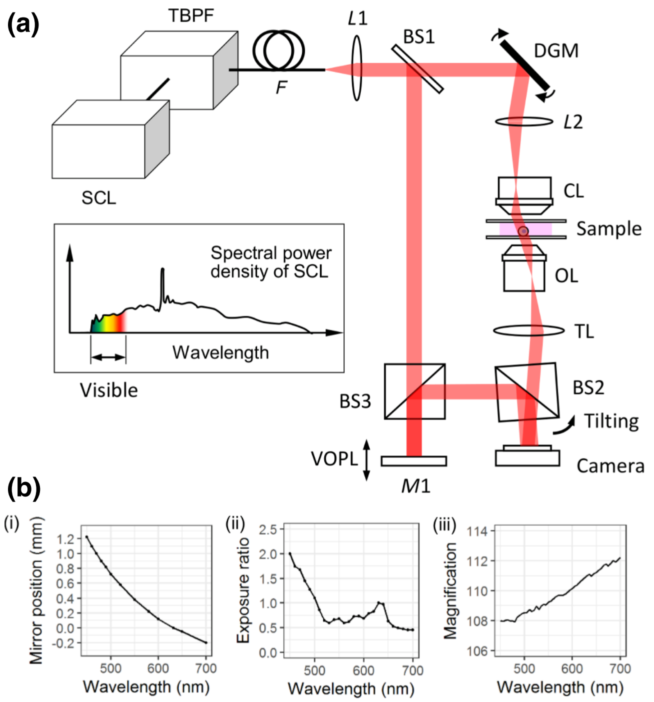

FIG. 1. Spectroscopic microtomography using DHT. (a) The setup. (b) Parameter setting for different wavelengths: (i) mirror position in the reference arm for variable optical path length (VOPL), (ii) exposure time normalized by the value for 632 nm, and (iii) magnification change. BS1, BS2, and BS3, beam splitters; CL, condenser lens; DGM, dual-axis galvanometer mirror; F, optical fiber; L1 and L2, lenses; M1, mirror; OL, objective lens; SCL, supercontinuum laser; TBPF, tunable bandpass filter; TL: tube lens

straight fringes [19]. For each wavelength, we record 200 images for various angles of incidence onto the sample. The angle of incidence is changed with two galvanometer scanners (Cambridge Technology, 8310KM60) installed at intermediate image planes. The maximum angle of incidence is 50° with respect to the optical axis. With variation of the angle of incidence, the direction and spacing of the interference fringes changes in the recorded raw images. For hyperspectral imaging, the wavelength is scanned from 450 to 700 nm with a 5-nm step size. We record the images using a 14-bit charge-coupled-device camera (Allied Vision, Pike F-421B) with 2048 × 2048 pixels of 7.4-μm pixel size. The pixel resolution is 0.067 μm, and the largest field of view is 136 × 136 μm^2. The imaging resolution of DHT has been well characterized [14]; it is twice the coherent diffraction limit (i.e., about 0.2 μm in the transverse plane and 0.4 μm in the vertical plane, with the exact value depending on the wavelength).

Using a Michelson interferometer, we measure the coherence length of the laser light after the tunable filter, which is about 20 μm at 632 nm. With a Mach-Zehnder interferometer, the current design requires the optical-path difference between sample and reference arms to be less than the coherence length. As the sample beam and the reference beam propagate through different optical elements, their optical path lengths vary differently as the wavelength is scanned. To compensate for this difference, the reference arm is made to have variable optical path length with use of beam splitter BS3 and mirror M1 mounted on a motorized stage (Thorlabs, MTS50-Z8). With use of the motorized stage with 50-mm travel range and 1.6-μm bidirectional repeatability, high fringe visibility can be achieved for all the measured wavelengths. The position of M1 providing the highest fringe visibility at a wavelength of 632 nm is found by our moving the mirror across the entire travel range. Then mirror M1 is moved from −0.2 to 1.2 mm as the wavelength is scanned from 450 to 700 nm as shown in Fig. 1(b)(i). The laser power at the fiber end as well as the transmittance of optical components varies with the wavelength. To maximize the signal strength while preventing pixel saturation, we adjust the camera exposure time as shown in Fig. 1(b)(ii). Because of the chromatic aberration, the imaging magnification slightly changes as the wavelength is scanned. Figure 1(b)(iii) shows the magnification change, which is estimated with use of the projected area of the bead. We use LabVIEW (National Instruments, version 15) for synchronous control of the tunable filter, the two galvanometer mirrors, the motorized stage in the reference arm, and the camera. For each specimen, we acquire 10 200 interferograms (51 wavelength steps and 200 images for each wavelength), which takes about 15 min without optimization. The camera frame rate limits the data-acquisition speed of the current system. The data-acquisition speed can be significantly increased with use of a complementary-metal-oxide-semiconductor camera [20]. Before the experiment, we acquire one set of background images, (i.e., the images without the sample in the field of view). The background images are subtracted from the sample images acquired later to compensate for nonuniform illumination and optical aberration.

Polystyrene beads (undyed, blue dyed, and red dyed) of 10-μm diameter were purchased from Phosphorex (118, 1010KB, and 1010KR). Index-matching liquid of refractive index 1.560 (at 589.3 nm and 25°) was purchased from Cargille (1809X). The refractive-index dispersion curve for the liquid was provided by the manufacturer and used in the data processing. The transmittance, also provided by the manufacturer, was 100% for all the measured wavelengths and the sample thickness. For imaging single red blood cells (RBCs), a drop of blood is obtained from a healthy adult donor and mixed in a 1.5-ml tube with 1 ml of 1× phosphate-buffered saline (PBS; Corning, 21-040-CV) without calcium and magnesium. For oxygenated RBCs, 20 μl of blood solution is pipetted out from the tube, mixed with the same volume of PBS on a glass coverslip, and covered with another coverslip. The deoxygenated RBC sample is prepared similarly except PBS is replaced with 2% sodium metabisulfite (Sigma, 799343-500G) dissolved

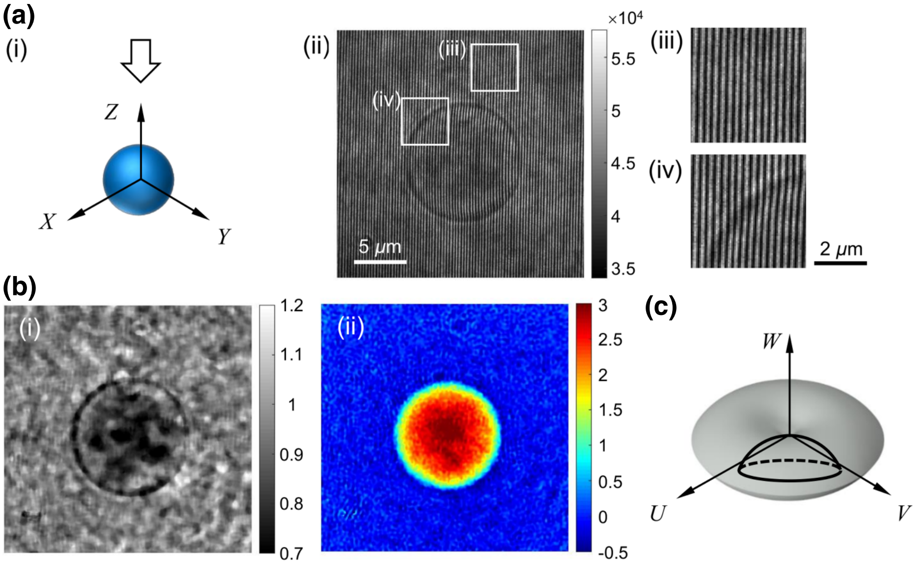

FIG. 2. Data processing in DHT. (a) The coordinate system (i) used for the analysis and an example raw image (ii) of a 10-μm blue-dyed polystyrene bead at 600-nm wavelength. Enlarged images of two regions in (ii) are shown in (iii) and (iv). (b) The complex scattered field—that is, the amplitude (i) and phase (ii)—extracted from the interferogram. (c) Mapping of the complex scattered field onto the Ewald sphere, which is shown as solid lines. (U, V, W) are the spatial-frequency components corresponding to (X, Y, Z), where X and Y are the transverse coordinates in the sample space and Z represents the optical axis.

in distilled water [21]. The experimental protocol using human blood was approved by the Institutional Review Board at the University of Wisconsin-Milwaukee.

Figure 2(a) shows an example raw image of a blue-dyed polystyrene bead at 600-nm wavelength. The two regions in the field of view, magnified on the right, show that the sample-induced phase alteration modulates the fringe pattern. The change in image intensity can be related to the sample's absorption, although it is not clearly seen in the raw interferogram. Figure 2(b) shows the amplitude (i) and phase (ii) images extracted from the raw interferogram with a standard fringe-analysis technique [19]. The amplitude image is contaminated with speckle noise; however, it clearly shows highly nonuniform absorption by the blue-dyed bead. The phase image, on the other hand, shows smooth phase variation, which is proportional to the bead's surface profile. The other raw interferograms are similarly processed to generate the amplitude and phase images corresponding to different viewing angles and wavelengths. The scalar diffraction theory simplified with the first-order Born or Rytov approximation [22] relates the measured scattered field to the object's scattering potential. The first-order Born approximation is more appropriate when the sample is thin, whereas the first-order Rytov approximation is more accurate when the sample is thick but the refractive-index jump at discrete boundaries is small [14]. This condition is fulfilled in all our imaging experiments; the maximum refractive-index contrast is about 0.03 for the real part and 0.002 for the imaginary part. For each wavelength, the complex scattered fields (i.e., the amplitude and phase images) are mapped onto the Ewald sphere in the three-dimensional spatial-frequency space [22]. For example, the solid line in Fig. 2(c) represents the boundary of the Ewald sphere, onto which the complex scattered field, Fig. 2(b), corresponding to zero incidence angle is mapped. The gray region in Fig. 2(c) represents the support of the object's three-dimensional spatial-frequency spectrum after the mapping is complete. The three-dimensional inverse Fourier transform of the spatial-frequency spectrum provides the object's scattering potential, and thus the complex-refractive-index map in three dimensions. The real part of the complex refractive index is simply called the "refractive index," and the imaginary part is called the "absorption constant" k. The absorption constant can be converted to the absorption coefficient μ_a, which is widely used in absorption spectroscopy, by $\mu_a = (4\pi/\lambda)k$. Because of the finite numerical aperture of the lenses, angle-scan tomography does not sample some spatial-frequency components near the origin of the coordinates. The missing-cone region, which is also seen in Fig. 2(c), distorts the image along the axial direction and underestimates the refractive index. Several regularization techniques (see, e.g., Refs. [23–26]), have been proposed to alleviate this problem. Full recovery of the missing-cone region is still a challenging and important task for future studies. This contrasts with well-studied missing-angle problems where the angular spectrum is uniformly undersampled [27,28].

III. RESULTS AND DISCUSSION

Using the spectroscopic microtomography system, we image three types of polystyrene beads (undyed, blue dyed, and red dyed) and single RBCs (oxygenated and deoxygenated) in the wavelength range from 450 to 700 nm. Figure 3 compares the refractive-index [Fig. 3(a)] and the absorption-constant [Fig. 3(b)] tomograms of a blue-dyed bead at two different wavelengths: 450 and 600 nm. As expected, the bead exhibits different refractive-index values at the two wavelengths, while strong absorption is observed only at 600 nm, one of the absorption peaks. The distribution of the refractive index within the bead

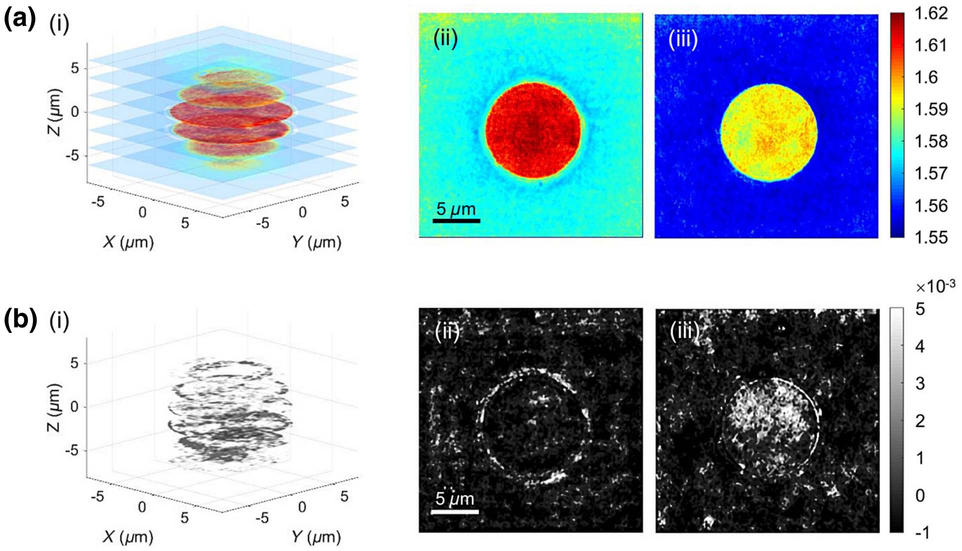

FIG. 3. Example tomographic reconstruction of a 10-μm blue-dyed polystyrene bead: the real (a) and imaginary (b) parts of the complex-valued refractive index. In (a),(b), multiple horizontal cross sections at 2-μm interval are shown in (i), and (ii) and (iii) show the center cross sections at 450 nm and 600 nm, respectively.

is uniform, whereas that of the absorption constant is nonuniform, possibly due to the laser speckle noise and heterogeneous distribution of the dye. In DHT, absorption measurement is more sensitive to laser speckle noise than the phase measurement. This may be because the absorption is directly extracted from the intensity of the raw interferogram, whereas the phase information is obtained from the fringe distortion. Figure 4(a) compares the probability density of the refractive index within the center cross section for different wavelengths (450, 520, and 600 nm) and different types of beads (undyed, blue dyed, and red dyed) . The regularization algorithm increases the accuracy of refractive-index measurement [23]; thus, the peak position or the average refractive index is accurate. The FWHM of each peak is, however, as broad as 0.01, which is attributed to the remaining missing-cone artifact. Figure 4(b) compares the probability density of the absorption constant for the different wavelengths and bead types. The absorption constant is on the order of 0.001, which is much smaller than the refractive index. Despite different widths, each probability-density distribution has a distinct peak, which is shifted to the right when the bead absorbs light of a specific wavelength.

Figure 5(a) compares the refractive index for the three types of beads in the wavelength range from 450 to 700 nm. For each bead type, we measure five beads. The graph shows the mean value, with the error bar representing one standard deviation. Figure 5(b) compares the absorption coefficients, with the shaded bands representing one standard deviation. The standard deviation is nonuniform

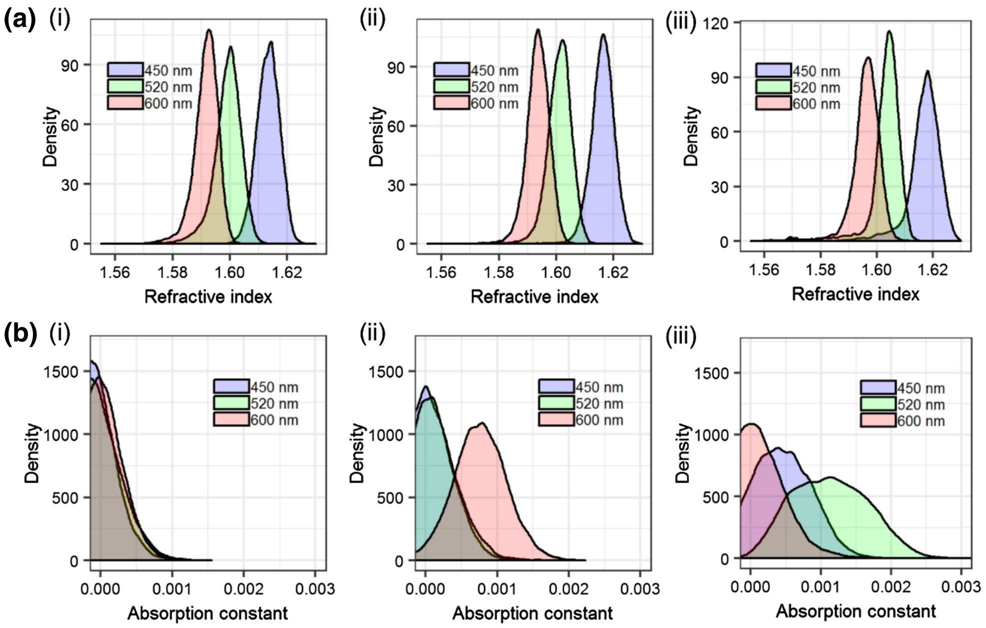

FIG. 4. Probability density of refractive index (a) and absorption constant (b) within the reconstructed bead. The results for undyed, blue-dyed, and red-dyed polystyrene beads are shown in (i), (ii), and (iii), respectively. Each graph compares the distributions for three different wavelengths: 450, 520, and 600 nm.

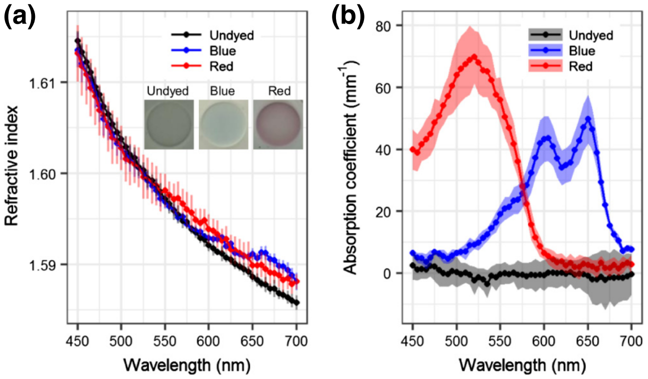

FIG. 5. Spectroscopic microtomography of three types of polystyrene beads (undyed, blue dyed, and red dyed): (a) refractive index and (b) absorption coefficient.

across the wavelengths, which may be attributed to the variation of the laser power and the fringe visibility at different wavelengths. In Fig. 5(a), the refractive-index profile for undyed beads matches well with the refractive-index dispersion of bulk polystyrene [29]. The refractive-index profiles for blue-dyed and red-dyed beads slightly deviate from the refractive-index profile for undyed beads due to the absorption peaks seen in Fig. 5(b). The absorption-coefficient distributions are significantly different from each other and well represent the characteristics of dyes. The blue-dyed beads have two absorption peaks: 43 ± 7 mm^{-1} at 605 nm and 50 ± 8 mm^{-1} at 650 nm. The red-dyed beads have one absorption peak: 70 ± 9 mm^{-1} at 520 nm. The exact dye types are unknown (bead-manufacturer proprietary information).

Figure 6(a) compares the refractive index of 11 oxygenated and six deoxygenated single RBCs in the wavelength range from 450 to 700 nm. The refractive index is shown as the increment from the value at 700 nm. For oxygenated RBCs, the refractive-index profile shows small peaks near 545 nm and at 580 nm, which were also observed for oxygenated hemoglobin solutions [2,16–18]. The refractive index of oxygenated RBCs decreases by 0.011 ± 0.003 as the wavelength increases from 450 to 700 nm. The amount of increase is comparable to some of the previously reported values (e.g., 0.004 [16] and 0.018 [17]) but is significantly greater than another previously reported value (0.001 [18]). In the deoxygenated (with sodium metabisulfite) group, we observe two types of cells with distinct morphology: spheroidal and flat. The refractive-index increment matches well with the previous results obtained with a subtractive Kramers-Kronig analysis for deoxygenated hemoglobin solutions [16]. The refractive index of deoxygenated RBCs decreases by 0.015 ± 0.002 as the wavelength increases from 450 to 700 nm. This is also comparable to a previously reported value (0.012) for deoxygenated hemoglobin solutions [16]. Figure 6(b) compares the absorption coefficient of 11 oxygenated and six deoxygenated single RBCs in the same wavelength range. The absorption spectra for oxygenated and deoxygenated single RBCs match well with previous absorbance measurements on hemoglobin solutions [16,17,30] and single RBCs [31]. For oxygenated RBCs, the hemoglobin Q bands are clearly seen at 540 and 575 nm. The absorption coefficients at the observed peaks are 48.6 ± 7.7 mm^{-1} at 540 nm and 52.1 ± 6.3 mm^{-1} at 575 nm. For deoxygenated RBCs, the two bands are fused to form one peak at 555 nm, at which the absorption coefficient is 49.0 ± 4.7 mm^{-1}.

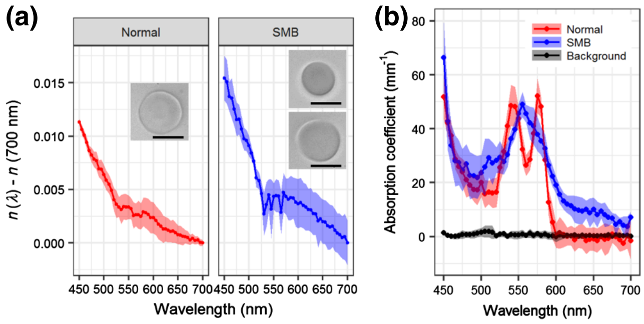

FIG. 6. Spectroscopic microtomography of oxygenated and deoxygenated single RBCs: (a) refractive-index increment with respect to the value at 700 nm and (b) absorption coefficient. "Normal" refers to the oxygenated RBCs, "SMB" refers the RBCs deoxygenated with sodium metabisulfite, and "background" refers to the value in the medium. The scale bar in (a) is 5 μm.

DHT using the refractive index as imaging contrast has been explored as a minimally invasive, label-free tool for imaging and quantification of some biological processes. This study demonstrates the potential of DHT using absorption as imaging contrast. Figures 5 and 6 clearly show the advantage of absorption measurement when the sample's absorption is not negligible. The refractive-index profiles decrease monotonically in most of the wavelength range, and the values are not much different among different bead types or between oxygenated and deoxygenated RBCs. In contrast, the absorption profiles clearly distinguish the three different types of beads and the RBCs in different oxygenation states. The refractive index and absorption coefficient of RBCs are important parameters determining the absorption and scattering properties of a living tissue [32,33]. While existing spectrophotometers can provide the average absorption coefficient of a homogeneous sample by assuming its thickness, the method demonstrated here can directly measure the absorption coefficient of a heterogeneous specimen with unknown height. Single-cell imaging and spectroscopy of RBCs have been shown to reveal intriguing mechanochemical coupling (mechanically induced cell deoxygenation) [31,34], which was not observed in a bulk measurement. As DHT is nondestructive and does not require any special sample preparation, the same specimen can be further analyzed with complementary techniques, including nuclear-magnetic-resonance spectroscopy, Raman spectroscopy, fluorescence spectroscopy, or atomic force microscopy [35].

ACKNOWLEDGMENTS

This research was funded by the Lynde and Harry Bradley Catalyst Program. We gratefully acknowledge NKT Photonics for the loan of a supercontinuum laser and a tunable filter, and helpful feedback from Dr. Kirkwood Pritchard and Deron Jones at the Medical College of Wisconsin.

[1] U. Morgner, W. Drexler, F. X. Kärtner, X. D. Li, C. Pitris, E. P. Ippen, and J. G. Fujimoto, Spectroscopic optical coherence tomography, Opt. Lett. **25**, 111 (2000).

[2] Francisco E. Robles, Lisa L. Satterwhite, and Adam Wax, Nonlinear phase dispersion spectroscopy, Opt. Lett. **36**, 4665 (2011).

[3] Irving Itzkan, Le Qiu, Hui Fang, Munir M. Zaman, Edward Vitkin, Ionita C. Ghiran, Saira Salahuddin, Mark Modell, Charlotte Andersson, and Lauren M. Kimerer, Confocal light absorption and scattering spectroscopic microscopy monitors organelles in live cells with no exogenous labels, Proc. Natl. Acad. Sci. USA **104**, 17255 (2007).

[4] J. Dudak, J. Zemlicka, J. Karch, Z. Hermanova, J. Kvacek, and F. Krejci, Microtomography with photon counting detectors: Improving the quality of tomographic reconstruction by voxel-space oversampling, J. Instrum. **12**, C01060 (2017).

[5] M. Obst, J. Wang, and A. P. Hitchcock, Soft X-ray spectrotomography study of cyanobacterial biomineral nucleation, Geobiology **7**, 577 (2009).

[6] Michael C. Martin, Charlotte Dabat-Blondeau, Miriam Unger, Julia Sedlmair, Dilworth Y. Parkinson, Hans A. Bechtel, Barbara Illman, Jonathan M. Castro, Marco Keiluweit, and David Buschke, 3d spectral imaging with synchrotron Fourier transform infrared spectromicrotomography, Nat. Methods **10**, 861 (2013).

[7] Vladimir Bobroff, Hsiang-Hsin Chen, Maylis Delugin, Sophie Javerzat, and Cyril Petibois, Quantitative IR microscopy and spectromics open the way to 3D digital pathology, J. Biophotonics **10**, 598 (2017).

[8] Vincent Lauer, New approach to optical diffraction tomography yielding a vector equation of diffraction tomography and a novel tomographic microscope, J. Microsc. **205**, 165 (2002).

[9] Florian Charriere, Anca Marian, Frederic Montfort, Jonas Kuehn, Tristan Colomb, Etienne Cuche, Pierre Marquet, and Christian Depeursinge, Cell refractive index tomography by digital holographic microscopy, Opt. Lett. **31**, 178 (2006).

[10] Wonshik Choi, Christopher Fang-Yen, Kamran Badizadegan, Seungeun Oh, Niyom Lue, Ramachandra R. Dasari, and Michael S. Feld, Tomographic phase microscopy, Nat. Methods **4**, 717 (2007).

[11] Taewoo Kim, Renjie Zhou, Mustafa Mir, S. Derin Babacan, P. Scott Carney, Lynford L. Goddard, and Gabriel Popescu, White-light diffraction tomography of unlabelled live cells, Nat. Photon. **8**, 256 (2014).

[12] Lei Tian and Laura Waller, 3d intensity and phase imaging from light field measurements in an LED array microscope, Optica **2**, 104 (2015).

[13] P. Bon, S. Aknoun, J. Savatier, B. Wattellier, and S. Monneret, Tomographic incoherent phase imaging, a diffraction tomography alternative for any white-light microscope, Proc. SPIE **8589**, 858918 (2013).

[14] Yongjin Sung, Wonshik Choi, Niyom Lue, Ramachandra R. Dasari, and Zahid Yaqoob, Stain-free quantification of chromosomes in live cells using regularized tomographic phase microscopy, PLoS ONE **7**, e49502 (2012).

[15] JaeHwang Jung, Kyoohyun Kim, Jonghee Yoon, and YongKeun Park, Hyperspectral optical diffraction tomography, Opt. Express **24**, 2006 (2016).

[16] Dirk J. Faber, Maurice C. G. Aalders, Egbert G. Mik, Brett A. Hooper, Martin J. C. van Gemert, and Ton G. van Leeuwen, Oxygen saturation-dependent absorption and scattering of blood, Phys. Rev. Lett. **93**, 028102 (2004).

[17] Moritz Friebel and Martina C. Meinke, Determination of the complex refractive index of highly concentrated hemoglobin solutions using transmittance and reflectance measurements, J. Biomed. Opt. **10**, 064019 (2005).

[18] Martin Hammer, Dietrich Schweitzer, Bernhard Michel, Eike Thamm, and Achim Kolb, Single scattering by red blood cells, Appl. Opt. **37**, 7410 (1998).

[19] K. Creath, Phase-measurement interferometry techniques, Prog. Opt. **26**, 349 (1988).

[20] Christopher Fang-Yen, Wonshik Choi, Yongjin Sung, Charles J. Holbrow, Ramachandra R. Dasari, and Michael S. Feld, Video-rate tomographic phase microscopy, J. Biomed. Opt. **16**, 011005 (2011).

[21] Toshio Asakura and John Mayberry, Relationship between morphologic characteristics of sickle cells and method of deoxygenation, J Lab. Clin. Med. **104**, 987 (1984).

[22] Max Born and Emil Wolf, *Principles of Optics: Electromagnetic Theory of Propagation, Interference and Diffraction of Light* (Cambridge University Press, Cambridge, 2013).

[23] Yongjin Sung and Ramachandra R. Dasari, Deterministic regularization of three-dimensional optical diffraction tomography, J. Opt. Soc. Am. A **28**, 1554 (2011).

[24] JooWon Lim, KyeoReh Lee, Kyong Hwan Jin, Seungwoo Shin, SeoEun Lee, YongKeun Park, and Jong Chul Ye, Comparative study of iterative reconstruction algorithms for missing cone problems in optical diffraction tomography, Opt. Express **23**, 16933 (2015).

[25] Ulugbek S. Kamilov, Dehong Liu, Hassan Mansour, and Petros T. Boufounos, A recursive Born approach to nonlinear inverse scattering, IEEE Signal Process. Lett. **23**, 1052 (2016).

[26] Ulugbek S. Kamilov, Ioannis N. Papadopoulos, Morteza H. Shoreh, Alexandre Goy, Cedric Vonesch, Michael Unser, and Demetri Psaltis, Optical tomographic image reconstruction based on beam propagation and sparse regularization, IEEE Trans. Comput. Imaging **2**, 59 (2016).

[27] Michael Lustig, David Donoho, and John M. Pauly, Sparse MRI: The application of compressed sensing for rapid MR imaging, Magn. Reson. Med. **58**, 1182 (2007).

[28] Guang-Hong Chen, Jie Tang, and Shuai Leng, Prior image constrained compressed sensing (PICCS): A method to accurately reconstruct dynamic CT images from highly undersampled projection data sets, Med. Phys. **35**, 660 (2008).

[29] Nina Sultanova, S. Kasarova, and I. Nikolov, Dispersion proper ties of optical polymers, Acta Phys. Pol. A **116**, 585 (2009).

[30] W. G. Zijlstra, A. Buursma, and W. P. Meeuwsen-van der Roest, Absorption spectra of human fetal and adult oxyhemoglobin, de-oxyhemoglobin, carboxyhemoglobin, and methemoglobin, Clin. Chem. **37**, 1633 (1991).

[31] Michal Wojdyla, Saurabh Raj, and Dmitri Petrov, Absorption spectroscopy of single red blood cells in the presence of mechanical deformations induced by optical traps, J. Biomed. Opt. **17**, 097006 (2012).

[32] Andre Roggan, Moritz Friebel, Klaus Drschel, Andreas Hahn, and Gerhard J. Mueller, Optical properties of circulating human blood in the wavelength range 400–2500 nm, J. Biomed. Opt. **4**, 36 (1999).

[33] A. N. Yaroslavsky, I. V. Yaroslavsky, T. Goldbach, and H. J. Schwarzmaier, The optical properties of blood in the near infrared spectral range, Proc. SPIE **2678**, 314 (1996).

[34] Satish Rao, Stefan Balint, Benjamin Cossins, Victor Guallar, and Dmitri Petrov, Raman study of mechanically induced oxygenation state transition of red blood cells using optical tweezers, Biophys. J. **96**, 209 (2009).

[35] Charilaos Mousoulis, Xin Xu, David A. Reiter, and Corey P. Neu, Single cell spectroscopy: Noninvasive measures of small-scale structure and function, Methods **64**, 119 (2013).